doi:10.1246/cl.2010.1226

Highlight Review

Tailoring Material Properties through Defect Engineering

Harry L. Tuller* and Sean R. Bishop

(Received April 27, 2010; CL-108007)

Abstract

Many advanced materials today derive their function from precise control of point defects. Through manipulation of point defects, the electrical, optical, mechanical, and other properties of materials can be systematically modified and optimized. This feature paper illustrates the type of progress that has been made in understanding the often complex equilibria exhibited by many materials and shows, by use of examples, how this knowledge can be applied to tailor materials' properties through defect engineering. Examples which highlight key points of defect engineering include: dark conductivity of radiation detectors, chemomechanics and nanoionics of solid oxide fuel cell materials, sensitivity of high frequency resonators for high-temperature mass measurements, and emission lifetime and luminescence intensity of phosphor materials.

◆ Introduction

The functioning of our modern world depends on our ability to modify and optimize, for example, the electrical, optical, and mechanical properties of a wide class of functional materials. These properties are often strongly dependent on the nature, concentration, and arrangement of defects of various dimensionality e.g., pores, grain boundaries, dislocations, impurities, vacancies, etc. While covalent materials such as Si and GaAs have received the lion's share of attention, given their critical importance in electronic and photonic devices, ionically bonded materials are receiving growing interest given their importance in energy conversion and storage devices (fuel cells and batteries), as sensors and actuators, and as high K dielectrics and ferroelectrics, just to name a few. In these types of solids, zero-dimensional, or point defects play a particularly important role in influencing properties. A key objective of this feature paper is 1) to illustrate the progress that has been made in understanding the often complex defect equilibria exhibited by many of these materials and 2) to show how this knowledge can be applied to tailor materials' properties through *defect engineering*.

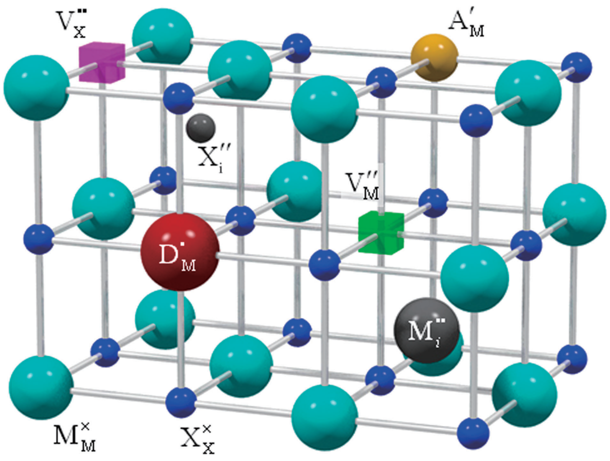

Figure 1. Depiction of types of point defects that can occur in a rock salt structured $M^{+2}X^{-2}$ compound.

To begin with, we introduce the key types of point defects, shown schematically in Figure 1, for the compound MX where M is a metal such as Ni or Na and X is an anion such as O or Cl. These include missing ions from lattice sites (vacancies: V_X and V_M), ions occupying interstitial crystallographic sites (interstitials: M_i and X_i), and donor (D_M) and acceptor (A_M) substitutional impurities. Other types of less common defects (not shown) include interstitial impurities (D_i and A_i) and anti-site disorder (M_X and X_M). The defect elements are described by Kröger–Vink notation,[1] where the first letter denotes either an atom or vacancy, the subscript specifies the site in the lattice, and the superscript describes the charge with respect to the lattice (×: neutral, ′: negative, and •: positive). For example, $M_M^{\times}$ is an M^{2+} atom located on an M^{2+} site (neutral charge with respect to the crystal lattice), while, $M_i^{\bullet\bullet}$ is an M^{2+} atom located on a normally neutral interstitial site and thus has a net charge of 2+. Defects form intrinsically at elevated temperatures for entropic reasons, commonly in pairs, in order to maintain crystal site stoichiometry and overall electrical charge neutrality. These include Schottky (V''_M–$V_X^{\bullet\bullet}$), Frenkel (V''_M–$M_i^{\bullet\bullet}$), and anti-Frenkel (X''_i–$V_X^{\bullet\bullet}$) defect pairs. Other defects are formed due to loss or gain of M or X by reaction with the gas phase (nonstoichiometry) or in response to the incorporation of aliovalent impurities (i.e., donors or acceptors). Examples are illustrated in the ensuing paper.

◆ Radiation Detectors: Electrical Conductivity

A common means of detecting nonvisible and visible light is with photoconductors. When a photon with energy exceeding the band gap is absorbed, an electron–hole pair is generated, contributing to an increase in the electrical conductivity. Thus the total conductivity becomes the sum of the conductivity in the dark plus the incremental part due to photon absorption, i.e.,

---

Prof. Harry L. Tuller and Dr. Sean R. Bishop*
Department of Materials Science and Engineering, Massachusetts Institute of Technology, 77 Massachusetts Avenue, Cambridge, MA 02139-4307, USA
E-mail: tuller@mit.edu

$\sigma_{\mathrm{tot}} = \sigma_{\mathrm{dark}} + \Delta\sigma_{\mathrm{ph}}$. A key figure of merit, or sensitivity, improves as σ_{dark} decreases and as $\Delta\sigma_{\mathrm{ph}}$ increases, the latter a function of the electron/hole mobility-lifetime product. γ-Ray detectors, working on the same principle, sometimes utilize ionic-bonded materials such as TlBr.[2,3] Here the γ-rays stopped by the heavy Tl and Br ions, generate electron–hole pairs which contribute to an increase in conductivity proportional to the incident radiation flux, assuming a low enough dark conductivity. Given that the dark conductivity appears to be largely ionic in TlBr,[4] it is necessary to establish the defect equilibria and ionic transport characteristics before choosing the most effective means for reducing the dark conductivity.

Dark conductivity can occur in TlBr through conduction of Tl or Br vacancies that exist intrinsically as Schottky pairs described earlier or introduced extrinsically through aliovalent doping. The first step in elucidating the contribution of each defect to dark conduction is the determination of which defect has the higher mobility. Ionic conductivity for defect i is given by

$$\sigma_{\mathrm{i}} = |z_{\mathrm{i}}| q \mu_{\mathrm{i}} [\mathrm{i}] \tag{1}$$

in which $z_{\mathrm{i}}q$ is the charge, [i] the carrier concentration, and μ_{i} the mobility of defect i. The total conductivity is the sum of conductivities for each defect species. In the extrinsic region, the addition of charged dopants largely fixes the concentration of the oppositely charged defect carrier, similarly to n or p type doping in semiconductor electronics. For example, doping with a known amount of S^{2-} on the Br site, at reduced temperature, fixes the concentration of Br vacancies, i.e., $[\mathrm{S}_{\mathrm{Br}}'] = [\mathrm{V}_{\mathrm{Br}}^{\bullet}]$. This allows the mobility to be extracted, with assistance of eq 1, from a measurement of *bulk*, or grain, conductivity.

The mobility of ions is proportional, via the Nernst–Einstein equation, to their diffusivity. Thus, the ion mobility depends on the readiness with which it can “jump” from one site, through a *bottleneck*, to an equivalent empty site in the lattice. The energy (ΔG_{m}) needed to overcome the barrier, depends on a number of factors including the strain energy required to distort the lattice during its transition as well as electrostatic interactions between the ion and the lattice as schematically depicted in Figure 2. Given its activated nature, the ionic mobility follows an Arrhenius relationship with temperature as

$$\mu_{\mathrm{i}} = \frac{\mu_{\mathrm{i,o}}}{T} \exp\left(-\frac{H_{\mathrm{m}}}{kT}\right) \tag{2}$$

where k is the Boltzmann constant, T is temperature, H_{m} is the enthalpy of migration, and entropy is contained in the pre-exponential, $\mu_{\mathrm{i,o}}$.

In the temperature region where the mobile defect concentration is fixed by dopants, the slope and intercept of $\log(\sigma T)$ versus $1/T$ yields H_{m} and $\mu_{\mathrm{i,o}}$, respectively (combining eqs 1 and 2). This is shown in Figure 3 for S (acceptor: compensated by $\mathrm{V}_{\mathrm{Br}}^{\bullet}$) and Pb (donor: compensated by $\mathrm{V}_{\mathrm{Tl}}'$)-doped TlBr.[5] From the figure, it is apparent that $\mathrm{V}_{\mathrm{Br}}^{\bullet}$ has a considerably higher mobility than $\mathrm{V}_{\mathrm{Tl}}'$, because the S-doped case displays the higher conductivity for the given concentration of dopant (100 ppm). At higher temperatures, the material reverts to the intrinsic condition where Schottky defect equilibrium dominates given by the following defect expressions:

$$0 \rightleftharpoons \mathrm{V}_{\mathrm{Tl}}' + \mathrm{V}_{\mathrm{Br}}^{\bullet} \tag{3}$$

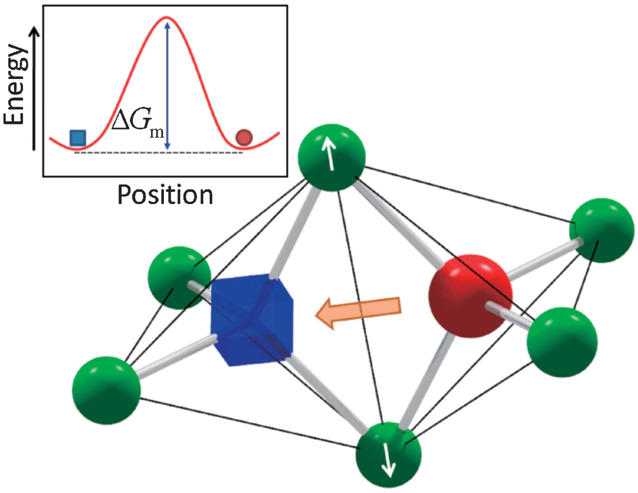

Figure 2. Illustration of the energy required for an ion to “jump” from one site to an equivalent, vacant site.

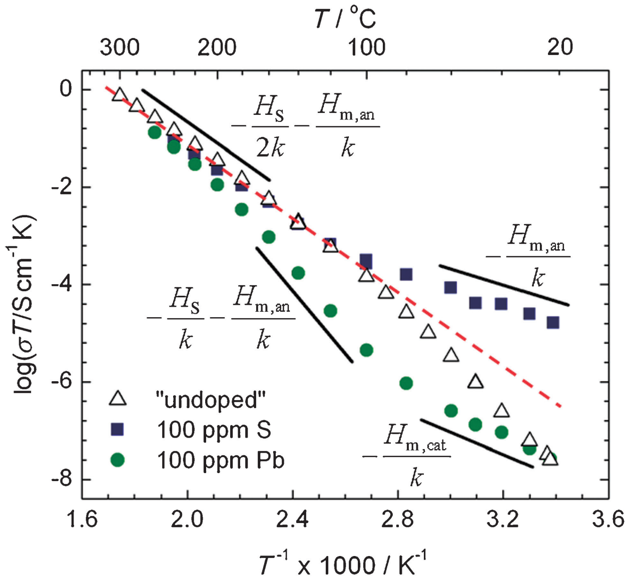

Figure 3. Intrinsic and extrinsic ionic conductivity in TlBr.[5] Dashed line indicates extrapolation of intrinsic regime to low temperature. Solid lines represent slopes used to determine defect formation and migration energies.

$$[\mathrm{V}_{\mathrm{Tl}}'][\mathrm{V}_{\mathrm{Br}}^{\bullet}] = k_{\mathrm{S}} \exp\left(-\frac{H_{\mathrm{S}}}{kT}\right) \tag{4}$$

In the intrinsic regime, $[\mathrm{V}_{\mathrm{Tl}}'] = [\mathrm{V}_{\mathrm{Br}}^{\bullet}]$ and so the slope in Figure 3 is given by $-(H_{\mathrm{S}}/2 - H_{\mathrm{m,an}})/k$ since anion vacancies have the higher mobility and, therefore, dominate the total conductivity. Interestingly, the extrinsic region in the Pb (donor)-doped case exhibits two different temperature dependent regimes. In both temperature regimes, the Pb dopant fixes $[\mathrm{V}_{\mathrm{Tl}}']$ while $[\mathrm{V}_{\mathrm{Br}}^{\bullet}]$ is rapidly changing with an activation energy of H_{S}. However, at intermediate temperature, the $\mathrm{V}_{\mathrm{Br}}^{\bullet}$ conductivity still dominates the total conductivity given that the mobility of $\mathrm{V}_{\mathrm{Tl}}'$ is orders of magnitude lower than that of $\mathrm{V}_{\mathrm{Br}}^{\bullet}$.

This yields the steep slope dependence shown in Figure 3 for the data designated by solid, green circles at intermediate temperature. In addition to the Pb-doped case, the "undoped" sample (open, blue triangles) displays a similar slope at low temperature, suggesting the existence of unintentional donor impurities. With the dashed, red line in Figure 3 corresponding to the intrinsic conductivity of TlBr, one finds that donor additions can be used to reduce the total dark conductivity below even the extrapolated room-temperature intrinsic conductivity by at least an order of magnitude. Thus, a knowledge and understanding of the defect chemistry provides a means for improving a key *figure of merit* of TlBr detectors, the dark conductivity.

◆ *Solid Oxide Fuel Cells (SOFCs): Chemomechanics*

The rising demand for energy precludes the use of technologies that consume resources in an unsustainable manner. SOFCs generate electricity from the direct electrochemical oxidation of fuel, thereby overcoming inefficiencies and minimizing emissions typical of traditional combustion methods.[6] A key figure of merit is low internal resistance, achieved, in part, by the use of highly oxide ion conductive materials for the solid electrolyte. Fluorite-structured oxides such as yttria-stabilized zirconia (YSZ) or gadolinia-doped ceria (GDC) achieve high oxide ion conductivity at elevated temperatures by the substitution with very high concentrations (ca. 10–20 mol %) of acceptor ions (Y^{3+} or Gd^{3+}) on the host crystal cation site (Zr^{4+} or Ce^{4+}).[7,8] Such high levels of dopants and oxygen vacancies can lead to dopant-defect association or ordering with a negative impact on oxygen vacancy mobility.[9]

Defects are also formed due to interactions of solids with the gas phase. Ceria, for example, becomes highly oxygen-deficient under reducing conditions, e.g., when heated in low oxygen partial pressure (P_{O_2}) atmospheres, typical of the fuel side of the SOFC.[10] The reduction reaction and the corresponding mass action relation are given by

$$O_O^{\times} \rightleftharpoons V_O^{\bullet\bullet} + 2e' + 1/2O_2(g) \qquad (5)$$

$$[V_O^{\bullet\bullet}]n^2 P_{O_2}{}^{1/2} = K_R(T) = k_R \exp(-E_R/kT) \qquad (6)$$

in which oxygen exits the lattice, leaving behind a doubly charged oxygen vacancy and two free electrons.[11]

This complicates its use as an SOFC solid electrolyte since reduction contributes to electronic conductivity and a consequent reduction in the fuel cell open-circuit voltage. Additionally, ceria displays significant dilation upon reduction resulting from a combination of repulsive forces between charged defects no longer separated by oxide ions as well as changes in neighboring ionic radii.[10,12] This *chemomechanics* effect can contribute to warping and delamination of SOFC structures and ultimately to mechanical failure, as depicted in Figure 4, if not properly taken into account.[13,14]

Due to the impact that changes in stoichiometry can have on mechanical and electrical effects, it is important to develop predictive models applicable over a wide range of temperature, P_{O_2}, and dopant concentration. The intrinsic ionic disorder in fluorite-structured oxides such as ceria is anti-Frenkel and follows the temperature dependence,[15]

$$0 \rightleftharpoons V_O^{\bullet\bullet} + O_i'' \qquad (7)$$

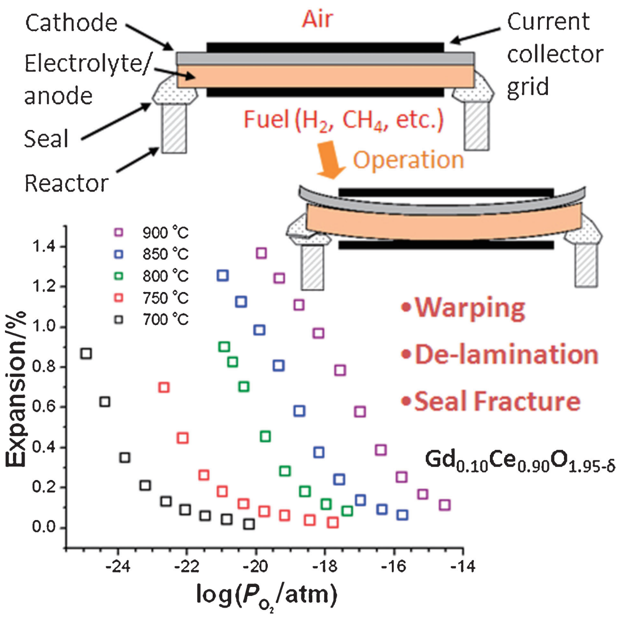

Figure 4. Illustration of chemical expansion effect on SOFC operation with experimental data for Gd-doped ceria modified from ref 10.

$$[V_O^{\bullet\bullet}][O_i''] = K_{AF}(T) = k_{AF} \exp(-E_{AF}/kT) \qquad (8)$$

In addition to the formation of intrinsic ionic defects, free electrons and holes can be generated across the band gap via

$$0 \rightleftharpoons e' + h^{\bullet} \qquad (9)$$

$$np = K_e(T) = k_e \exp(-E_g/kT) \qquad (10)$$

The addition of aliovalent dopants provides another level of control. Since overall charge needs to be conserved in the lattice, a charge neutrality equation is introduced

$$n + 2[O_i''] + [A'_{Ce}] = p + 2[V_O^{\bullet\bullet}] \qquad (11)$$

Provided that the defect formation energies and their corresponding pre-exponents are known, each defect concentration can be determined as a function of P_{O_2}, T, and $[A'_{Ce}]$, given that there are four unknowns and four independent equations. Though such equations can be solved numerically, it is useful to make certain approximations such that they are readily solved.[16] One method, the Brouwer approximation[17] has been used to delineate regions in the isothermal plot of defect concentration versus P_{O_2}, or defect equilibrium diagram (DED), shown in Figure 5. Here, experimental conditions are selected in which only one type of charged defect on each side of the equality sign in eq 11 is dominant. For example, at very low P_{O_2} (region I in Figure 5), $V_O^{\bullet\bullet}$ and e' form in large concentrations according to eq 6. As a consequence, O_i'' and $h^{\bullet}$ are markedly depressed, conforming to the mass action equations of 8 and 10, respectively. Therefore, from eq 11, $[V_O^{\bullet\bullet}] \approx 1/2n$, which can be substituted into eq 6 to yield $1/2n \approx [V_O^{\bullet\bullet}] \propto P_{O_2}^{-1/6}$. This P_{O_2} dependence for $V_O^{\bullet\bullet}$ and e' is exemplified in region I of Figure 5.

At higher P_{O_2}, the acceptor dopant is the dominant negative defect and so $[V_O^{\bullet\bullet}] \approx 1/2[A'_{Ce}]$, which can be substituted into eq 6 to yield $n \propto P_{O_2}^{-1/4}$. It is apparent from the DED that ceria remains predominantly ionic only in region II, known as the electrolytic region or domain. In all other regions, the

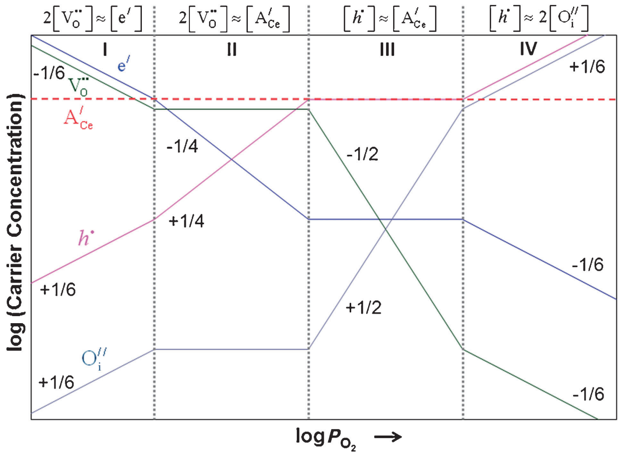

Figure 5. Defect equilibrium diagram for an acceptor-doped fluorite oxide such as ceria.

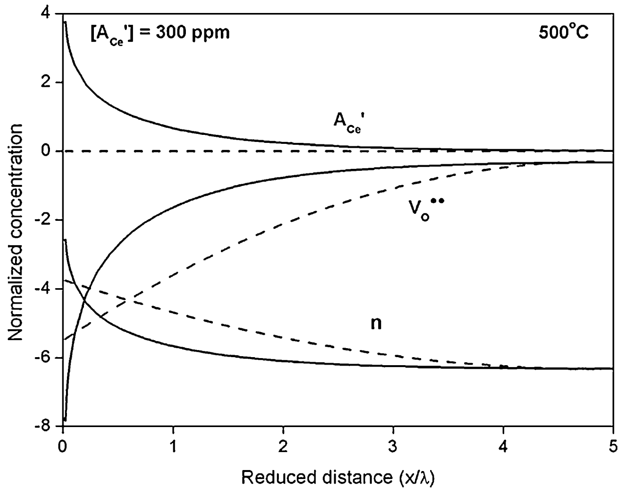

Figure 6. Defect concentration profiles according to Gouy–Chapman (solid lines) and Mott–Schottky (dotted lines) models for a space charge potential of 0.4 V and an acceptor concentration of 300 ppm at 500 °C. Reproduced with permission of the PCCP Owner Societies.[26]

approximate electroneutrality condition includes electrons or holes as majority carriers and therefore ceria displays mixed ionic electronic conduction. By adding $[\mathrm{A'_{Ce}}]$, the electrolytic region is extended to lower P_{O_2} which improves the ceria electrolyte performance in an SOFC environment.[18] Nevertheless, an optimum doping concentration exists since, as discussed above, the $\mathrm{V_O^{\bullet\bullet}}$ mobility exhibits a maximum with $[\mathrm{A'_{Ce}}]$ concentration, above which defects interact resulting in decreased $\mathrm{V_O^{\bullet\bullet}}$ conductivity and, hence, an increase in the relative electronic contribution. Reducing the operating temperature also broadens the electrolytic region because electronic carrier generation by either generation across the band gap or by reduction (eqs 10 and 6) are typically more strongly activated than the ionic mobility (eq 2). Therefore, through the combination of optimum doping and temperature operation, doped ceria can be used as a high-performance SOFC electrolyte. The electrodes in an SOFC, on the contrary, benefit in performance from the existence of mixed ionic and electronic conduction. For example, mixed conduction supports fuel oxidation over the full surface area of a ceria-based anode because of the presence of both free electrons and oxide ions required for the reaction. This condition is satisfied as one approaches region I at the reduced P_{O_2} conditions experienced at the anode of the SOFC.

The effect of defect formation on internally developed strains and how these, in turn, affect conductivity and mechanical stability is of increasing interest. Lattice strain can affect mobility by narrowing or widening the lattice bottleneck (Figure 2) for atoms to transfer through. New studies in this field of electrochemomechanics are underway in an effort to fundamentally understand the interplay between these components and the role that defects play in them. For example, doping may change the degree of "reducibility" of these materials and hence lead to ways to mitigate or even enhance the *chemical coefficient of expansion*.

◆ *SOFCs: Nanoscale Effects*

In an attempt to extend the operating life and reduce costs of SOFCs, there has been an increasing focus on reducing the electrolyte resistance by substantially reducing its thickness through switching from bulk ceramics or thick films to thin films.[19,20] Indeed, solid electrolyte membranes of ca. 150 nm thickness would provide adequate electrolyte conductance down to temperatures of 200 and 400 °C with GDC and YSZ, respectively.[21,22] Such thin films, commonly characterized by features with nanosized grain size, often exhibit unique features, including dramatic changes in defect concentrations as compared to the same materials with micron-sized grains. The author and co-workers first reported that the electrical conductivity of bulk nanocrystalline CeO_2 increased substantially over that of coarsened microcrystalline CeO_2, due in that case, to increased electronic conductivity.[23] This was subsequently attributed to space charge effects resulting from segregation of positive charges to the grain boundary cores.[24,25] Expressing the change in space charge concentration $c_i(x)$ of defect species i relative to its bulk concentration $c_{i\infty}$ as a function of the local electrical potential $\Delta\phi(x)$ gives the following equation.[26]

$$\left(\frac{c_i(x)}{c_{i\infty}}\right)^{1/z_i} = \exp\left(-\frac{e}{kT}\Delta\phi(x)\right) \qquad (12)$$

Defect concentration profiles, predicted using eq 12 and Poisson's equation, for two types of approximations, Gouy–Chapman (mobile dopant) and Mott–Schottky (immobile dopant), are plotted in Figure 6 for the predominant defects in ceria. Under these conditions, very significant depletion of oxygen vacancies and enhancement of electrons are predicted in response to a positive potential in the grain boundary core. While such space charge effects are expected to occur at grain boundaries in large grain materials as well, their impact on conduction parallel to the grain boundaries is minimal because the space charge widths are typically on the order of nanometers in these highly doped materials. However, as the grain size approaches tens of nanometers, then the impact of defect accumulation and depletion along grain boundaries can take on a dominant role, as in nanosize-grained ceria. Through *grain boundary engineering*, the electrical properties can be significantly modified and as such, this technique is now being pursued by the authors.[26,27] Here, selectively doping the grain boundary region, so as to change the magnitude and sign of the space charge potential is utilized to control defect concentrations in the nanocrystalline solid, as opposed to the homogeneous doping commonly used in single crystals or large grain polycrystalline materials as discussed above. As an example, doping with an acceptor at the grain boundary is expected to reduce the positive potential of the grain boundary core and thus enhances the grain boundary ionic conductivity, beneficial to SOFC electrolytes.

♦ High-frequency Resonators: High-temperature Stability

Langasite ($La_3Ga_5SiO_{14}$), like quartz, is piezoelectric and can be used to fabricate single crystal high-frequency resonators. In contrast to quartz, which goes through a destructive phase transition at 573 °C, langasite, remains a stable piezoelectric up to its melting point of 1470 °C.[28] As a consequence, it has an excellent potential for serving as a high temperature resonating crystal mass balance.[29,30] In this application, a film sensitive to the chemical analyte in the gas phase is applied to the crystal. For example, as the gas adsorbs onto or absorbs into the film, its mass changes resulting in a shift in the resonant frequency of the resonator. Several key figures of merit for such devices must be satisfied to insure high mass sensitivity at elevated temperatures and controlled atmospheres. First, the resonator must be low loss to yield a high quality factor and thus high mass resolution. While this is readily obtained at room temperature, where langasite is highly resistive ($>10^{12}\,\Omega\,\mathrm{cm}$), with increasing temperature, the resistivity drops exponentially and could become problematic at the elevated temperatures where its application as a mass nanobalance is of interest. Thus, as with TlBr, the defect and transport properties must be understood in order to be in a position to create a strategy to increase langasite's resistivity to as high a level as possible at desired operating temperatures. Second, as we learned above, oxides such as langasite can gain or lose mass by exchange of oxygen with the gas phase. This could lead to a substantial reduction of the balance mass resolution, as this mass change would compete with the mass change to be intentionally detected in the film.

A series of acceptor- and donor-doped langasite crystals were prepared, and their electrical conductivities were studied as functions of temperature and P_{O_2}. These results were analyzed in a fashion similar to that discussed above for TlBr conductivity and ceria defect equilibria to derive appropriate values for K_R, K_{AF}, and K_e along with carrier mobilities. On this basis, it became possible to predict the dependence of the total conductivity on dopant concentration, temperature, and P_{O_2}. An example is shown in Figure 7, in which the total electrical conductivity for langasite at 800 °C is shown plotted as a function of net acceptor minus donor density at P_{O_2} equal to 1, 10^{-10}, and 10^{-20} atm.[31]

While the lowest conductivity is obtained when langasite is intrinsic (i.e., negligible impurities), it is impractical to obtain such crystals. Alternatively, Figure 7 informs us that if a langasite resonator is to be used in the P_{O_2} range from 1 to 10^{-10} atm, a low concentration of donors will insure a lower conductivity than using acceptor dopants. However, under strongly reducing environments (e.g., $P_{O_2} = 10^{-20}$ atm), a low concentration of acceptor results in a lower conductivity than using donor dopants. Following a similar approach, the shift in frequency Δf of 0.25 Hz is expected of a bulk acoustic wave resonator fabricated from donor-doped (1 mol %) langasite operating at 10 MHz at 1000 °C, if the oxygen partial pressure changes from $P_{O_2} = 1$ to 10^{-10} atm due to generation of oxygen vacancies. This frequency shift is typically below the measurable resolution of the device (ca. 5 Hz) and, therefore, can be neglected in mass measurements. Thus, through proper selection of dopants, langasite can serve as a highly sensitive mass balance even at elevated temperatures and reducing atmospheres.

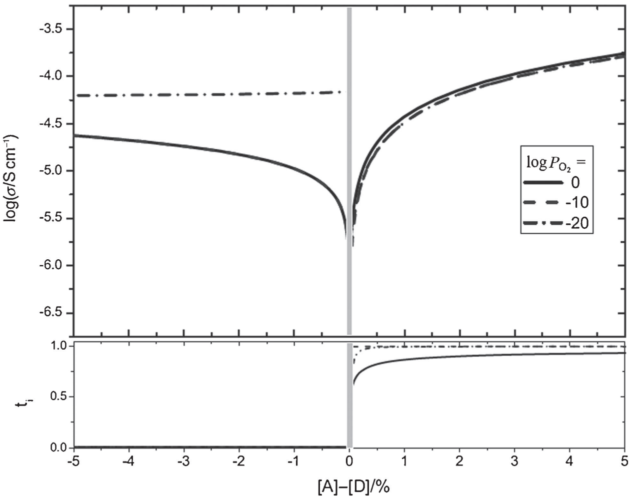

Figure 7. Conductivity and ionic transport (t_i) number prediction for langasite at 800 °C and three different P_{O_2}'s as a function of dopant level.[31]

♦ Displays: Phosphorescence

In this last example, we consider how an understanding of the defect properties can be used to optimize the characteristics of an important phosphor and laser material. Yttrium aluminum garnet[32] (YAG or $Y_3Al_5O_{12}$) single crystal is attractive as the crystalline host in solid-state lasers (e.g., Nd:YAG) due to its mechanical strength and broad optical window extending to −6 eV. Cerium-doped YAG is of interest as a fast response phosphor under e-beam excitation. Absorption bands obtained at 340 and 460 nm, are due to the 4f–5d transition of Ce^{3+} with an additional peak at 220 nm.[33] When Ce:YAG is pumped with an electron beam or with photon excitation at 266 nm, it emits at two wavelength bands, ca. 300 and 550 nm. The former peak is associated with a lattice defect, also found in undoped YAG, and the latter with the cerium dopant. Particularly interesting is that the intrinsic Ce-emission lifetime is found to increase from 70 ns to on the order of ms when an oxidized crystal is annealed in hydrogen.[34] This observed 800 ns "tail" superimposed on the 70 ns emission in photoluminescence is believed to result from energy transfer between the defect, which also exhibits an 800 ns lifetime, and the Ce^{3+} ion. The defect structure of YAG doped with a variety of dopants was extensively studied (e.g., Fe, Ni, Ca, and Ce) and the key thermodynamic and kinetic parameters derived.[33,35–37] With this insight, it was possible to understand the origin of the 800 ns "tail" and thereby control the emission lifetime as well as the luminescence intensity in Ce:YAG.

Summary

In this review, we explained how *defect engineering* can be used to advantageously modify electrical, mechanical, and optical properties in materials. In order to achieve this end, we described how systematic studies were performed to first characterize the material property in question as a function of environmental variables and then relate these properties back to populations of defects in the material using well-understood relationships. With this knowledge, the material's property can then be controlled by a combination of doping and proper selection of ambient conditions.

We thank the following organizations for their support: Radiation Monitoring Devices, Inc. and DNDO (for supplying input, TlBr samples, and funding: RMDC07-43), NSF (nanoceria DMR-0243993, langasite DMR-0908627 and DMR-0228787, YAG DMR-78-24185), and DOE-BES (SOFC chemo-mechanics DE SC0002633).

References and Notes

1 F. A. Kröger, H. J. Vink, *Solid State Physics: Advances in Research and Applications*, ed. by F. Seitz, D. Turnbull, Academic Press Inc., **1956**, Vol. 3, p. 307.
2 R. Hofstadter, *Phys. Rev.* **1947**, *72*, 1120.
3 A. V. Churilov, G. Ciampi, H. Kim, L. J. Cirignano, W. M. Higgins, F. Olschner, K. S. Shah, *IEEE Trans. Nucl. Sci.* **2009**, *56*, 1875.
4 G. A. Samara, *Phys. Rev. B* **1981**, *23*, 575.
5 S. R. Bishop, W. Higgins, G. Ciampi, A. Churilov, K. S. Shah, H. L. Tuller, *J. Electrochem. Soc.*, Submitted.
6 S. C. Singhal, K. Kendall, *High Temperature Solid Oxide Fuel Cells: Fundamentals, Design and Applications*, ed. by S. C Singhal, K. Kendall, Elsevier, Oxford, New York, **2003**.
7 B. C. H. Steele, *Solid State Ionics* **2000**, *129*, 95.
8 J.-H. Park, R. N. Blumenthal, *J. Electrochem. Soc.* **1989**, *136*, 2867.
9 J. A. Kilner, *Chem. Lett.* **2008**, *37*, 1012.
10 S. R. Bishop, K. L. Duncan, E. D. Wachsman, *Acta Mater.* **2009**, *57*, 3596.
11 In some cases viewed as reducing Ce^{4+} to Ce^{3+} ions.
12 S. R. Bishop, K. L. Duncan, E. D. Wachsman, *Electrochim. Acta* **2009**, *54*, 1436.
13 R. Krishnamurthy, B. W. Sheldon, *Acta Mater.* **2004**, *52*, 1807.
14 K. Sato, H. Omura, T. Hashida, K. Yashiro, H. Yugami, T. Kawada, J. Mizusaki, *J. Test. Eval.* **2006**, *34*, 12707.
15 T. G. Stratton, H. L. Tuller, *J. Chem. Soc., Faraday Trans. 2* **1987**, *83*, 1143.
16 K. L. Duncan, E. D. Wachsman, *Ionics* **2007**, *13*, 127.
17 R. A. Huggins, *Solid State Ionics* **2001**, *143*, 3.
18 H. L. Tuller, A. S. Nowick, *J. Electrochem. Soc.* **1975**, *122*, 255.
19 D. Beckel, A. Bieberle-Hütter, A. Harvey, A. Infortuna, U. P. Muecke, M. Prestat, J. L. M. Rupp, L. J. Gauckler, *J. Power Sources* **2007**, *173*, 325.
20 Z. P. Shao, S. M. Haile, J. Ahn, P. D. Ronney, Z. L. Zhan, S. A. Barnett, *Nature* **2005**, *435*, 795.
21 A. Bieberle-Hütter, J. L. Hertz, H. L. Tuller, *Acta Mater.* **2008**, *56*, 177.
22 H. Huang, M. Nakamura, P. Su, R. Fasching, Y. Saito, F. B. Prinz, *J. Electrochem. Soc.* **2007**, *154*, B20.
23 E. B. Lavik, I. Kosacki, H. L. Tuller, Y.-M. Chiang, J. Y. Ying, *J. Electroceram.* **1997**, *1*, 7.
24 S. Kim, J. Maier, *J. Electrochem. Soc.* **2002**, *149*, J73.
25 A. Tschöpe, *Solid State Ionics* **2001**, *139*, 267.
26 H. L. Tuller, S. J. Litzelman, W. Jung, *Phys. Chem. Chem. Phys.* **2009**, *11*, 3023.
27 S. J. Litzelman, R. A. De Souza, B. Butz, H. L. Tuller, M. Martin, D. Gerthsen, *J. Electroceram.* **2009**, *22*, 405.
28 A. A. Kaminskii, B. V. Mill, G. G. Khodzhabagyan, A. F. Konstantinova, A. I. Okorochkov, I. M. Silvestrova, *Phys. Status Solidi A* **1983**, *80*, 387.
29 H. Fritze, H. L. Tuller, *Appl. Phys. Lett.* **2001**, *78*, 976.
30 D. Damjanovic, *Curr. Opin. Solid State Mater. Sci.* **1998**, *3*, 469.
31 H. Seh, H. Fritze, H. L. Tuller, *J. Electroceram.* **2007**, *18*, 139.
32 Garnet refers to minerals with the general formula $A_3B_2(CO_4)_3$.
33 S. R. Rotman, H. L. Tuller, C. Warde, *J. Appl. Phys.* **1992**, *71*, 1209.
34 E. F. Gibbons, T. Y. Tien, R. G. DeLosh, P. J. Zacmanidis, H. L. Stadler, *J. Electrochem. Soc.* **1973**, *120*, 835.
35 S. R. Rotman, R. P. Tandon, H. L. Tuller, *J. Appl. Phys.* **1985**, *57*, 1951.
36 S. R. Rotman, H. L. Tuller, *J. Appl. Phys.* **1987**, *62*, 1305.
37 S. R. Rotman, H. L. Tuller, *Solid State Ionics* **1990**, *40–41*, 893.